A ternary EAM interatomic potential for U–Mo alloys with xenon

D E Smirnova[1,2]**, A Yu Kuksin**[1,3]**, S V Starikov**[1,3]**, V V Stegailov**[1,3]**,
Z Insepov**[2]**, J Rest**[2] **and A M Yacout**[2]

[1] Joint Institute for High Temperatures, Russian Academy of Sciences, Moscow 125412, Russia
[2] Argonne National Laboratory, Illinois 60439, USA
[3] Moscow Institute of Physics and Technology, Dolgoprudny 141700, Russia

E-mail: d.e.smirnov@gmail.com and starikov@ihed.ras.ru

Abstract

A new interatomic potential for a uranium–molybdenum system with xenon
is developed in the framework of an embedded atom model using a force-
matching technique and a dataset of *ab initio* atomic forces. The verification of
the potential proves that it is suitable for the investigation of various compounds
existing in the system as well as for simulation of pure elements: U, Mo
and Xe. Computed lattice constants, thermal expansion coefficients, elastic
properties and melting temperatures of U, Mo and Xe are consistent with the
experimentally measured values. The energies of the point defect formation in
pure U and Mo are proved to be comparable to the density-functional theory
calculations. We compare this new U–Mo–Xe potential with the previously
developed U and Mo–Xe potentials. A comparative study between the different
potential functions is provided. The key purpose of the new model is to study
the atomistic processes of defect evolution taking place in the U–Mo nuclear
fuel. Here we use the potential to simulate bcc alloys containing 10 wt% of
intermetallic Mo and U_2Mo.

(Some figures may appear in colour only in the online journal)

1. Introduction

Over the last several decades the problem of the development of new uraniferous fuel materials
has become extremely important because of the enhancement of technologies related to the
nuclear cycle implementation. One of the promising methods of further evolution of the nuclear
sector proposes using fast-neutron nuclear power reactors. The progress in reactor technology
encourages a search for fuel materials that can ensure a high level of efficiency along with a
operational safety.

Uranium alloys are under active investigation as possible fuels for future fast and research reactors [1–4]. Understanding the radiation damage effects on the fuel stability is one of the major challenges to be solved on the way to effective and safe fuel design. A description of radiation damage requires knowledge of the atomistic mechanisms of defect generation in solids [5–10]. In the case of uranium the radiation defect properties have still not been sufficiently studied either for pure U or for metallic uranium compounds, including U–Mo.

It has been experimentally proved that due to their good characteristics, uranium–molybdenum alloys are considered to be a prospective fuel material for fast neutron and research and test reactors [11]. Alloying pure high-temperature bcc γ-uranium with 5–20 wt% molybdenum with the following quenching produces dense γ-U–Mo structure that can be retained as metastable at $T = 300$–900 K, and then returns to a stable state with a rise in temperature ($T \geqslant 900$ K). Nevertheless, in both metastable and stable states the structure has appropriate mechanical and thermophysical properties [11–16] along with a heightened uranium density: 8–9 gU cm^{-3} for dispersion-type fuels and 15–18 gU cm^{-3} for monolithic fuel [17–20]. The last fact is important because it compensates for the low content of enriched uranium in the fuel. Meeting the conditions of high thermal conductivity, low thermal expansion, and stability under irradiation and corrosion resistance, U–Mo compositions also have low potential for interacting with cladding materials. All these points show the precedence of U–Mo over other examined high-dense metal fuels, for example, based on U-Zr [21]—also considered as an important fuel material for fast-neutron reactors [22]. The results of the theoretical comparison between the phase stability data for U–Mo and U–Zr provided in [23] also indicates the preference of γ-U–Mo due to an ability to remain in a bcc structure and corresponding very weak constituent redistribution in the typical fuel operation temperatures (compared with U–Zr, which undergoes several phase transitions).

However, the key problem hindering the use of these fuels in industry is insufficient knowledge about the stability of the γ-U–Mo composition against defect formation, swelling and possible phase transitions caused by heating, irradiation or the influence of fission products. Despite a number of reports discussing the experimental and theoretical study of the U–Mo system, the complete picture explaining the behaviour of U–Mo alloys under operation conditions is not clear at this time. To complete it one should take into account the possibility of structural and phase transitions, features of formation and redistribution of fission products, and the generation of radiation defects: vacancies, self-interstitial atoms (SIA), or even more complicated defect clusters and dislocations.

The molecular dynamics (MD) method was demonstrated to be useful for the investigation of mechanical and thermodynamical properties of various materials, processes of phase transitions, radiation-induced defect formation and evolution, displacement cascades and other structural changes caused by fission fragments. Therefore, the MD method can be very helpful for clarifying the phenomena indicated above or predicting some new aspects of U–Mo nuclear fuel performance. However, to apply MD to a chosen material an appropriate interatomic potential is required. For example, during the research on conventional uranium dioxide nuclear fuel (UO$_2$) dozens of interatomic potential models were introduced and then further improved [24–27]. Meanwhile, a review of the published interatomic potentials for U, Mo and their compounds leads us to conclude that at this time any research on the interatomic potential model for the U–Mo system has not been reported, even though this material is found to be very promising and suitable for advanced nuclear reactor technologies. Consequently, the goal of this work is to develop and then to verify the interatomic potential especially regarding the simulation and research of the structure and properties of the U–Mo system in various cases, including the problems dealing with the presence of gaseous fission fragments (using xenon as a generic example). In what follows, the explanations of the potential construction

scheme are given, the resulting potential functions are discussed and the potential verification is reported.

2. Construction of the potential

The construction of the interatomic potential for the ternary U–Mo-Xe system was performed within the framework of the embedded-atom method (EAM [28, 29]), allowing us to take into account many-particle interatomic interactions. This model is shown to be convenient in the cases of the binary Mo–Xe [30] system and pure uranium [31]. A general expression for the potential energy is chosen in the standard form:

$$U_i = \sum_{i<j} \varphi_{\alpha\beta}(r_{ij}) + F_\alpha(\overline{\rho_i}), \qquad \overline{\rho_i} = \sum_{j\neq i} \rho_\alpha(r_{ij}), \qquad \alpha, \beta = \text{U, Mo, Xe.} \qquad (1)$$

Here, the first term $\varphi_{\alpha\beta}$ is the pair potential depending on the distance r_{ij} between the two given atoms i and j (α and β are the element types). The second term F_α takes into account the many-body interatomic interactions. F_α depends on the effective electronic density $\overline{\rho_i}$ at the position where the ith atom is placed. For the ith atom, $\overline{\rho_i}$ is the sum over all contributions $\rho_\alpha(r_{ij})$ created by other jth atoms situated within the cut-off radius r_{cut} from the ith atom.

To design the EAM potential for a classical MD simulation of the system studied we use the force-matching method originally proposed by Ercolessi and Adams [32]. This technique provides the opportunity to construct reliable interatomic potentials even for complicated multicomponent systems by making use of the results of *ab initio* calculations. The idea is to adjust the set of the potential functions $\varphi_{\alpha\beta}(r)$, $\rho_\alpha(r)$ and $F_\alpha(\rho)$ to accurately reproduce per atom forces (together with energies and stresses) computed for some reference structures (so-called configurations) representing various phases existing in the system.

2.1. Preparing the reference configurations

In order to start the potential construction process it is necessary to prepare the reference configuration database to provide the basis for a new potential. In our case, to build a tool suitable for the simulation of a complicated ternary system (and each of its components separately) in a wide pressure and temperature range we have to prepare an extensive set of reference configurations representing all kinds of interesting structures. Each configuration is a small structure model corresponding to one of the possible states of the U–Mo–Xe system. It can represent a pure element (U, Mo, Xe) or a binary (U–Mo, Mo–Xe, U–Xe) and ternary (U–Mo–Xe) system at various given densities and temperatures. Temperature is regarded in this case as the parameter that provides the magnitude of the atomic displacements from the equilibrium states.

The model structure size here is strongly limited due to the high computational cost of the first-principles calculations. This means that the simulation box has a size less than or equal to 16 Å in each dimension and contains up to 250 atoms. The periodic boundary conditions (PBC) are applied in all three dimensions. For each of the reference structures we perform a short (∼1 ps) MD run at the given temperature T with some trial potential based on the EAM potentials [30, 31]. In general, the initial trial potential can be set rather arbitrarily but organization of the fitting procedure can lead to its improvement after every computational iteration. In this way we introduce the thermal displacements of atoms with the magnitudes reflecting the given temperature (which is necessary because for an ideal lattice with PBC the forces acting on the atoms equal zero). The final atomic arrangement after the MD calculation for a given initial structure is one of the required configurations. All classical MD computations reported in this work are performed using the LAMMPS code [33].

Table 1. Description of the configurations involved in the reference database.

Structure	n	Δ (%)	$P_{min}-P_{max}$ (GPa)	$V_{min}-V_{max}$ (Å^3/at)	$T_{min}-T_{max}$ (K)
Mo, bcc	27	21.6	−10–459	8.8–32	200–2900
Mo, liquid	4	19.2	3–52	14.5–17.08	2400–5200
α-U, orth	17	34.3	−3–98	15.1–24.8	450–2000
γ-U, bcc	9	31.8	−1–97	15.4–21	1000–3000
U, liquid	11	57.8	−1–102	15.5–33.2	2100–5900
γ-U–Mo, bcc	14	37.2	−5–62	15.5–21	300–1200
U–Mo–Xe, bcc	8	41.9	0–52	16.38–22	300–450
Mo–Xe, disordered	15	23.5	−2–396	11.2–66.8	200–2900
Mo–Xe, bcc	5	18.2	6–15	15	200–2900
Mo–Xe, fcc	1	29.4	50	24	50
Xe, fcc	4	39.5	1–82	14–52	50–130
Xe, disordered	6	51.3	0–8	41–182	800–1100
Defect structures					
SIA in solid Mo	8	—	1–5	15.5	300
Normalizing structures					
U, 4 at	1	—	0	539	—
Mo, 4 at	1	—	0	549.25	—
Xe, 4 at	1	—	0	503.67–732.3	—

*Note: n is the number of configurations of the given type. The minimum and maximum values of T, V, P chosen for each of the configuration types are given along with the average relative rms deviations (Δ, in %) between *ab initio* reference and EAM calculated forces, taken over all configurations of the given type.*

   The presence of U, Xe, Mo–Xe and Mo configurations prepared and tested during the work on the corresponding EAM potentials [30, 31] gives us the opportunity to use this set again without repeating the expensive *ab initio* computations. To expand the database and make it appropriate for the generation of a new combined U–Mo–Xe potential we additionally build configurations representing U with substitutional Xe atoms, binary bcc U–Mo alloys, and bcc U–Mo alloys with additional substitutional or interstitial Xe atoms.

   It should be noted that along with the configurations prepared to visualize some given structure at the given T, we additionally take into account so-called normalizing configurations. They are constructed manually for each pure element and represent the system containing several atoms placed in a cubic simulation box ($\sim$13 Å in size) in such a manner that the interatomic distances between them are larger than the given potential cut-off. The energy, stress and force values for every normalizing configuration are set to zero. This addition appears to be very useful because it helps us to meet the requirement of an embedded energy value of zero for every pure element (Xe, U or Mo) at zero electron density.

   The whole set of reference structures contains 132 configurations with various concentrations of U, Mo and Xe and at different given densities and temperatures T, together with normalizing data. Some explanations and general comments for the exact reference data set are given in table 1. For binary U–Mo models, the Mo concentration was chosen to be between 6 and 12 wt% to obtain a better reproduction of general nuclear fuel compositions. In two of the 'U–Mo–Xe' configurations $\sim$12% of all atoms of the initial bcc γ-U–Mo structure are substituted with Xe, while the other 6 'U–Mo–Xe' are bcc γ-U–Mo models with a single substitutional Xe atom together with a single uranium interstitial. An example of the latter is shown in figure 1(*b*) illustrating an idea of how the configurations involved appear. Figure 1 also contains an example of the pure Mo defect configuration (see figure 1(*c*)). A set of the structures expressing eight various point defect configurations was added to the database and
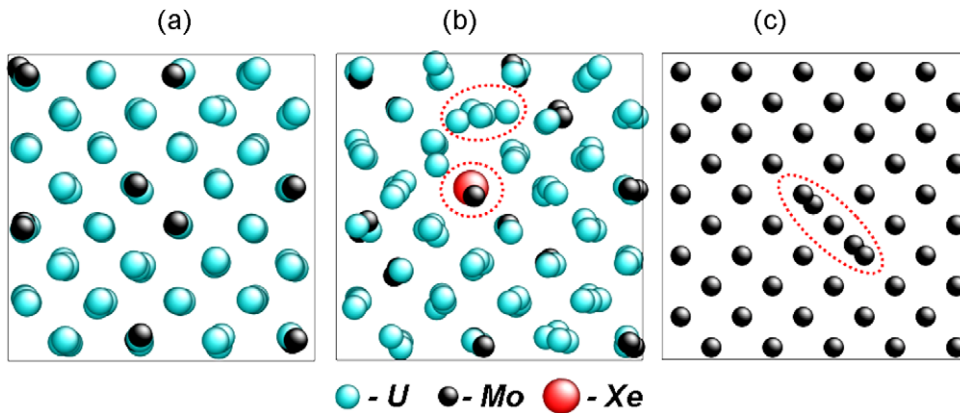
Figure 1. Examples of the configurations included in the reference data set. (*a*) γ-U–Mo bcc alloy (128 atoms, 8 at% of Mo, $T \sim 450$ K, $P = 16$ GPa); (*b*) U–Mo–Xe bcc configuration containing one substitutional Xe atom together with a single U interstitial (128 atoms, 12 at% of Mo, $T \sim 1200$ K, $P = 26$ GPa); (*c*) Mo bcc configuration with dumbbell $\langle 1\,1\,1 \rangle$ (D111) SIA (251 atoms, 300 K, 0 GPa). Positions of the structure defects existing in the last two configurations are denoted by the dotted circles.

took part in the following potential optimization. One can see that the fitting errors for the defect Mo structures are not denoted in table 1. This is caused by the non-conventional method of fitting applied to this part of the reference data. The explanation of this situation is given in the next subsection.

After the reference structure set was completed, the interatomic forces, energies and stresses for each configuration were calculated using the VASP [34] package (version 4.6). The projector augmented-wave (PAW) pseudopotentials together with the plane-wave basis cut-off energy of 400 eV are used. The Brillouin zone is sampled with a $3 \times 1 \times 2$ k-point mesh for orthorhombic α-U and a $2 \times 2 \times 2$ mesh for all bcc structures and liquid. The generalized gradient approximation of Perdew and Wang is used for the exchange-correlation functional.

2.2. Optimization of the potential functions

The optimization of the U–Mo–Xe EAM potential within the framework of the force-matching method based on the preliminary computed *ab initio* data was presented via the *potfit* program code [35]. The trial functions $\varphi_{\alpha\beta}$, ρ_α and F_α necessary for start of the computation procedure were composed from the previously reported and mentioned EAM potentials for pure U and binary Mo–Xe. One should also note that the functions defined previously for Mo–Mo, U–U, Mo–Xe and Xe–Xe interactions in [30, 31] were not fixed here during the *potfit* operations and could be changed to get a better representation of the ternary system. To sum up, the optimization procedure deals with 12 functions: 3 functions for ρ_α, 3 for F_α and 6 for pair potentials existing in the system. ρ_α and $\varphi_{\alpha\beta}$ were determined at the distances between the given r_{min} and r_{max}. The first value was set to be equal to the least interatomic distance available in the configuration set (1.5 Å) and r_{max} was set to be equal to a chosen potential cut-off distance (6.2 Å). The potential functions are represented by tabulated values (spline knots) and cubic spline interpolation. The spline knots are adjusted in an iterative way during the optimization procedure for minimizing the deviations between the reference database forces, energies and stresses, and the respective values calculated with the EAM potential. The fitting

errors between all the data involved are determined using a least-squares target function:

$$Z = Z_F + Z_C. \tag{2}$$

The first part (Z_F) is related to the difference between the EAM and *ab initio* forces calculated for N_a atoms listed in the reference database:

$$Z_F = \sum_{i=1}^{N_a} \sum_{\alpha=x,y,z} W_i \frac{(F_{i\alpha}^{EAM} - F_{i\alpha}^{DFT})^2}{(F_{i\alpha}^{DFT})^2 + \epsilon_i}, \tag{3}$$

and the second one gives the fitting errors for energy and stress values:

$$Z_C = \sum_{i=1}^{N_c} W_i \frac{(A_i^{EAM} - A_i^{DFT})^2}{(A_i^{DFT})^2 + \epsilon_i}. \tag{4}$$

Here $F_{i\alpha}$ are three force components acting on the given atom i, and W_i are the weights of different terms. A_i can be equal to the energy of the given configuration or to one of its six stress tensor components. N_c is the number of all reference energy and stress values. ϵ_i are the small values helping us to avoid extremely small denominators (and consecutive large meaningless contributions) when the reference value A_i^{DFT} is too small (although is known with a limited accuracy). The index 'DFT' denotes reference values; 'EAM'—computed with the fitted potential.

A specific case related to the features of the fitting process deals with the configurations containing given defects, i.e. eight molybdenum reference structures representing possible point-defect (vacancy and SIA) configurations. One of them (with an SIA dumbbell ⟨1 1 1⟩ defect) is depicted in figure 1(*c*). During the work on the EAM interatomic potential for the Mo–Xe system it was found out that accounting for high-pressure configurations with small interatomic distances does not lead automatically to an adequate representation of the defect properties. To obtain the potential aimed at the accurate simulation of the given defect structures it is necessary to include the examples of these structural defects in the reference database and achieve very high accuracy while fitting the corresponding energies because the differences between them are very small. If the *potfit* code is applied, this requirement can be met by assigning the substantially increased weights to the chosen defect structures, which means that the quality of the fitting in these cases will also improve. The separate weight values W_i attributed to every configuration taking part in the potential optimization procedure can be used to manage the process, for example, to achieve a better fit of some given phase (i.e. of its forces, energies and stresses). The default values for W_i equal 1, but for Mo defect configurations they were increased to 300–800. The forces per atom also presented for the delicate defect structures in the reference database should be excluded from the fitting procedure to avoid distorting the entire fitting by the outstanding weight values. The last problem can be solved again by means of the *potfit* code, which provides the opportunity to exclude the given indicated forces from the optimization processes. A number of optimization iterations were executed until we obtained the potential reproducing the initial *ab initio* data with the best possible accuracy. The precision of the force fitting can be appraised by calculating the relative root mean square deviations (RMSD):

$$\Delta = \frac{1}{N} \sum_{i=1}^{N} \sqrt{\frac{(F_i^{EAM} - F_i^{DFT})^2}{(F_i^{DFT})^2}}; \tag{5}$$

here N is the number of atoms in some given configuration, F_{EAM} is the force calculated with the EAM potential and F_{DFT} is the reference *ab initio* DFT force. The deviations $\triangle$ are computed for each atom in each configuration and then averaged within the given configuration
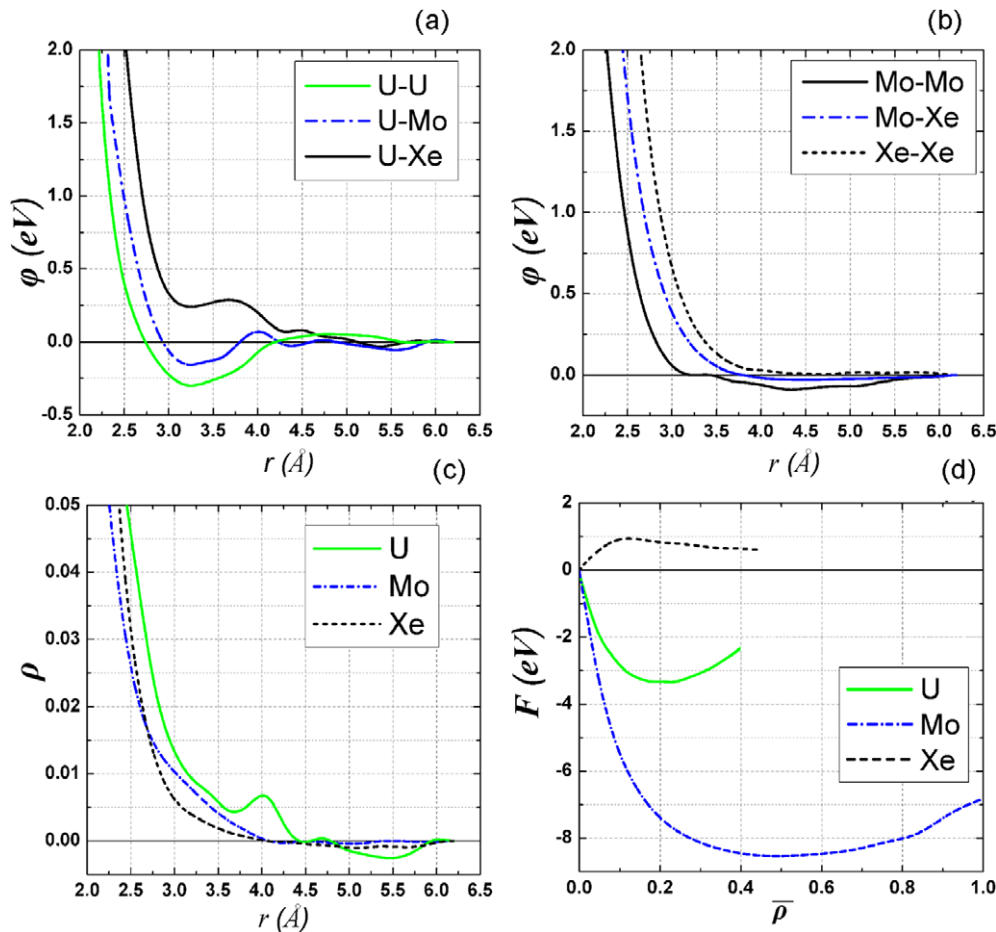
Figure 2. EAM potential functions derived via the *potfit* program code. Functions $\varphi_{\alpha\beta}(r)$ describing pair interactions between U, Mo and Xe are grouped together and plotted in figures (*a*) and (*b*); figure (*c*) shows the behaviour of electron densities $\rho(r)$; embedded functions $F(\overline{\rho})$ are shown in figure (*d*).

type for more compaction (see table 1). It should be mentioned here that the 20%–30% errors are typical values for the optimization techniques deployed [36]. The twelve functions defining the finally matched potential are grouped together and plotted in figures 2(*a*)–(*d*).

The potential functions have a number of peculiarities. For example, there is a local minimum of the U–Xe pair potential at $r = 3.2$ Å. Accordingly, one can suggest the presence of bonding between uranium and xenon. This last fact qualitatively agrees with the results of the experimental observations reported in [37]. From figure 2(*c*) one also might note that the resulting xenon electron density function appears to have negative values at distances from 4 to 6 Å. Such an occurrence arises from the organization of the *potfit* code, which permits the electron density functions to take negative values if it leads to a better EAM potential fitting (it was also observed for niobium [36]). An important point to be made here is that in the pressure–temperature area significant for solving practical problems dealing with xenon ($T > 250$ K and $0 < P < 100$ GPa) thermal fluctuations guarantee positive values for $\overline{\rho}$, preventing possible conflicts. At the same time, the relatively small r_{cut} chosen in this case leads to the fact that the
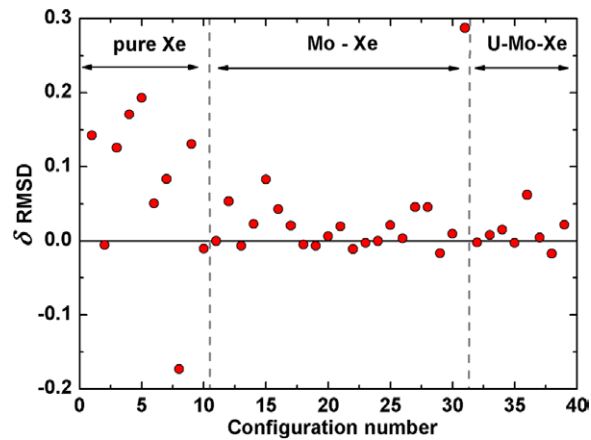
Figure 3. Relative root mean square deviations (RMSD) of fitted forces from the reference values for Xe, Mo–Xe and U–Mo–Xe configurations. δRMSD is equal to [RMSD(EAM$_1$) − RMSD(EAM$_2$)]/RMSD(EAM$_1$). Here EAM$_1$ is the original EAM U–Mo–Xe potential (plotted in figure 2), EAM$_2$ is the EAM U–Mo–Xe with $\rho_{Xe}(r_{ij})$ substituted from EAM Mo–Xe [30].

potential gives an insufficient description when applied to room-temperature xenon at normal density. But with an increase in the temperature (or density) of simulated xenon the quality of potential performance appears to be much better (see the verification subsection for the test results).

Trying to overcome the existence of negative $\rho_{Xe}(r_{ij})$, we perform additional optimizations in such a manner that all the functions dealing with U and Mo (plotted in figure 2) were kept fixed, and the Xe functions were varied. But these additional runs again result in a negative $\rho_{Xe}(r_{ij})$. Additionally, we try to replace $\rho_{Xe}(r_{ij})$ in developing EAM U–Mo–Xe with the function from the EAM Mo–Xe model [30] (which has a smaller negative region). However, this substitution makes worse the precision of the force fitting in cases dealing with pure Xe and Mo–Xe configurations (a comparison between the errors is provided in figure 3). The last result is understandable because the modification of the fully optimized potential set by including the function designed for the somewhat different system is not strongly valid; moreover, the function included has a smaller cut-off than the original one (5.6 Å versus 6.2 Å). To conclude, it should be said that while the efforts undertaken to eliminate the negative xenon electron density in developing the EAM U–Mo–Xe potential were not successful, it was decided to keep the obtained form of the function $\rho_{Xe}(r_{ij})$ with negative values in a range of interatomic distances. In particular, after the testing showed that the current version of the potential functions generally does not hinder the adequate reproduction of the xenon properties. The details of the simulation with the potential plotted in figure 2 are analysed below in the xenon verification subsection.

2.3. Analyses of the resulting potential functions for U–Mo–Xe in comparison with other potential models for U, Mo and Xe

Throughout all the above sections we often refer to the previously presented potentials developed for the pure U and binary Mo–Xe system [30, 31]. As was mentioned, the trial potential applied in this work was essentially based on these potentials. In addition, even the reference configuration data for the U–Mo–Xe system were in part inherited from those

computations. Therefore, it is reasonable to test the differences, if any, between the new EAM U–Mo–Xe potential functions and the previous results. Actually, the most convenient way of comparing different EAM potentials for the same element is the so-called effective pair format [38]. It is known that within the stated EAM formalism the energy U_i (see equation (1)) of the monoatomic model is invariant with respect to some transformations in which we modify the embedded function F_α of some element α by adding (or subtracting) a term linear in the electron density ρ_j:

$$G_\alpha(\overline{\rho}_\alpha) = F_\alpha(\overline{\rho}_\alpha) + k\overline{\rho}_\alpha \tag{6}$$

and, at the same time, adjust the pair potential φ_α as follows:

$$\psi_\alpha(r_{ij}) = \varphi_\alpha(r_{ij}) - 2k\rho_\alpha(r_{ij}), \qquad \alpha = \text{U, Mo, Xe}, \tag{7}$$

where $k = -\mathrm{d}F_\alpha/\mathrm{d}\overline{\rho}_\alpha$ at the given $\overline{\rho}_\alpha = \overline{\rho}_\alpha^0$, i.e. equilibrium electron density on atom corresponding to the chosen structure of the element α. The latter means that if we want to compare different EAM potentials using effective pair format it is necessary to choose values of $\overline{\rho}_\alpha^0$ related to the same structure in each of the potential cases. The methodology described was successfully applied for comparative study between the interatomic potentials for many elements, for example, Cu and Ag [39], and here we address it while investigating the results obtained for U, Mo and Xe in this work. It should be noted that recently other interatomic potentials for uranium were published [40–42].

As can be seen in figure 4, the potential functions representing interactions between uranium atoms in the initial potential [31] have not been changed significantly while processing the EAM U functions contained in the EAM U–Mo–Xe potential. In figure 4 the pair potentials from both of these models are presented (see figure 4(*a*)) together with the effective pair potentials derived for othorhombic α-U—figure 4(*b*) and for bcc γ-U—figure 4(*c*). The results of transformations applied to molybdenum EAM potentials are plotted in figure 5. From this figure the difference between pair potentials implemented in EAM U–Mo–Xe (line 1) and EAM Mo–Xe (line 2) models is seen, along with the fact that the effective pair format in general shows the consistence of both these models (see lines 3 and 4). In the case of pure xenon the difference between the studied pair potential is obvious (see lines labelled as 2 and 4), but after switching to the effective pair format form the EAM Xe potentials working in EAM U–Mo–Xe (line 3) and in EAM Mo–Xe (line 5) are found to be in good agreement. Moreover, comparison of the resulting curves with a widely used exponent-six pair potential for Xe [43] leads us to conclude that the shape of all these curves is quite close (see figure 6). The latter agrees well with the fact that the embedded function F of xenon is linear at the small $\overline{\rho}$ and, in other words, it means that the resulted Xe–Xe interaction defined by the EAM U–Mo–Xe potential is actually close to the pair-potential form, which appears to be sufficient to deal with xenon properties.

To sum up, it can be said that the analysis provided using effective pair format calculations shows some difference between U, Mo and Xe potential functions working in the different interatomic potentials. Nevertheless, the general view of all variants appears to be quite similar. To understand the full picture, these aspects should be analysed together with the particular potential verification results summarized in the corresponding sections of the work.

3. Application of the potential to simulation of pure elements: U, Mo and Xe

The following sections contain the summary of the U–Mo–Xe potential verification results.[4] Some test MD calculations of the structure, elastic constants, melting temperatures,

---

[4] The tabulated potential for U–Mo–Xe in the LAMMPS *setfl* format can be downloaded from the NIST interatomic potential repository (www.ctcms.nist.gov/potentials/).
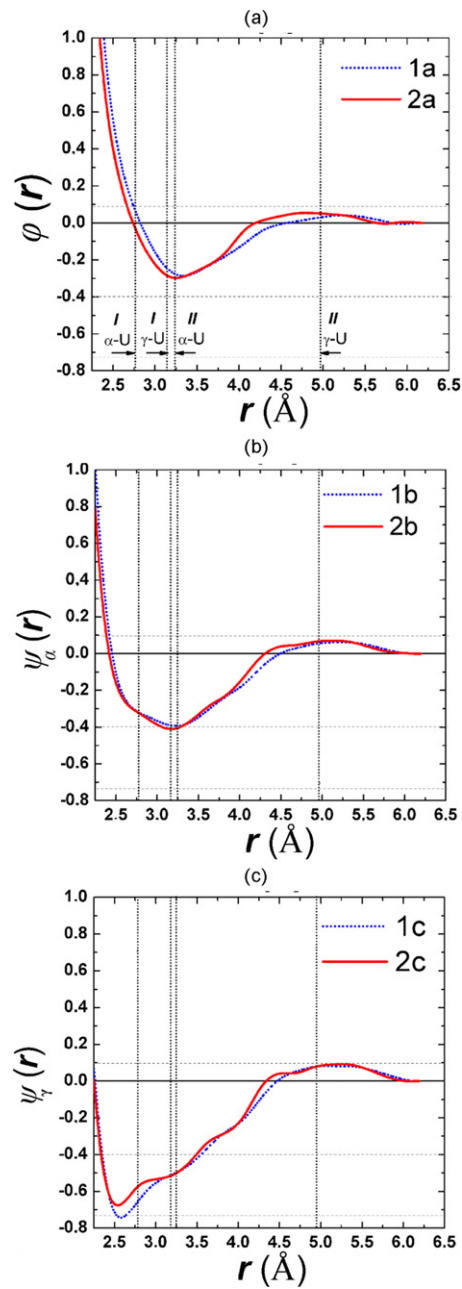
Figure 4. Uranium EAM potential functions presented in the effective pair format. Index '1' denotes functions related to EAM U [31]; 2—results of this work. Figure (*a*) shows the U–U pair potentials implemented in EAM U(1a) and in EAM U–Mo–Xe (2a). The next two figures describe the differences between the U EAM potential functions modified to the effective pair format for orthorhombic uranium (*b*) and bcc uranium (*c*). Vertical dotted lines indicate the coordinates of the first (I) and the second (II) peaks of uranium radial-distribution function calculated with EAM U–Mo–Xe for α-U at 300 K and for γ-U at 900 K.
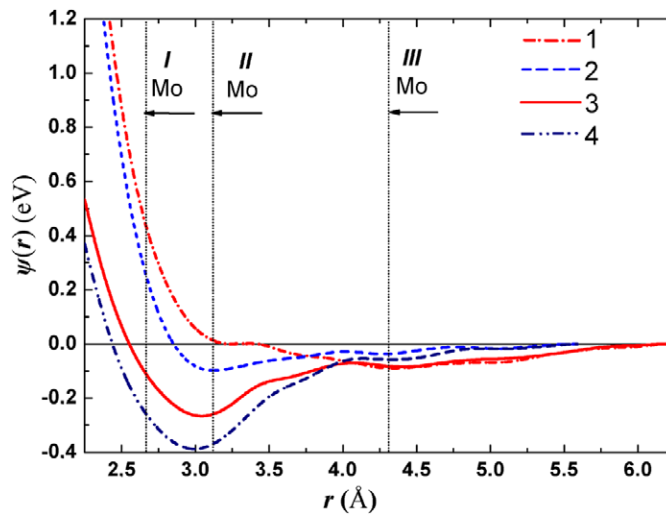
Figure 5. Comparison between Mo potential functions implemented in EAM U–Mo–Xe and EAM Mo–Xe. 1 and 2—Mo–Mo pair potentials ($\varphi_{\alpha\beta}(r)$) included in the EAM U–Mo–Xe and the EAM Mo–Xe [30] potentials respectively. 3 and 4—corresponding EAM Mo potentials in the effective pair format. Vertical dotted lines indicate the coordinates of the first (I), the second (II) and the third (III) peaks of bcc molybdenum radial-distribution function calculated with EAM U–Mo–Xe at 300 K.
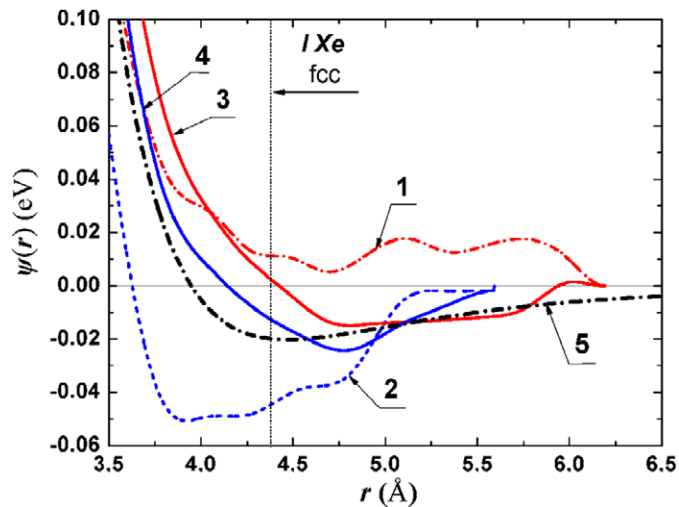

Figure 6. Results of the comparative study between various potentials for Xe. 1 and 2—Xe–Xe pair potentials ($\varphi_{\alpha\beta}(r)$) included in EAM U–Mo–Xe and EAM Mo–Xe [30], respectively. 3 and 4—corresponding Xe EAM potentials in the effective pair format calculated for compressed fcc Xe (at 50 GPa). 5—exp-6 potential for Xe [43], $r_{cut} = 14$ Å. Vertical dotted line indicates the coordinate of the first (I) peak of radial-distribution function calculated with EAM U–Mo–Xe for fcc Xe at 50 K.

room-temperature isotherms and other properties of pure U, Mo and Xe are accomplished, and the information obtained is compared with the known experimental and theoretical data. A comparison between the new results and those predicted previously by the U [31] and Mo–Xe potentials [30] is provided throughout the subsections.

Table 2. General characteristics of solid uranium phases in comparison with the existing experimental data and results calculated previously using MD with potential [31].

	EAM, this work	EAM U [31]	Experiment
		α-U	
a	2.854	2.8361	2.8537, 2.8540
b	5.751	5.7604	5.8695, 5.8700
c	4.944	4.9551	4.9548, 4.9550
y	0.1025	0.1015	0.1025
c_{11}	134.5	151	215
c_{22}	253	218	199
c_{33}	320	330	267
c_{12}	84.5	109	46
c_{13}	103	130	22
c_{23}	82	108	108
B	109	149	104, 135.5, 149
		γ-U	
a	3.542	3.493	3.53
B	92	95	113.3
$T_{\rm m}$	1530	1440	1408

Note: Lattice constants (a,b,c) are given in Å, bulk modulus and elastic constants (B, c_{ij}) of solid uranium phases are in GPa and melting temperature $T_{\rm m}$ is in K. The experimental values correspond to $T = 300$ K for α-U and ~900 K for γ-U. MD calculations are performed at the same temperatures. Lattice constants for α-U are taken from [76] (the first value) and [20] (the second value); c_{ij} are given in [77]; three different values of experimentally measured bulk modulus B of α-U are cited from [47, 49, 78], respectively. Data for γ-U are given in [47].

3.1. Calculation of pure uranium properties

For uranium crystal structures we calculate general characteristics that could be evidentially compared with the data measured in the experiments. The results are summarized in table 2. As can be seen, the bulk modulus of α-U agrees well with the existing experimental data. Elastic constants are within 20–40% of the experimental points. In the case of non-diagonal components c_{12} and c_{13}, disagreement is more significant. The melting temperature of U was computed by the two-phase simulation technique. This method implies work with a simulation box containing two coexisting phases (in our case: solid bcc and liquid uranium) with the interphase boundary between. The simulation box contains 19315 atoms of U at zero pressure. Similar simulations were previously successfully applied to other materials, and a detailed description of the calculation procedure can be found elsewhere [43–46]. Results of this test show that the potential predicts uranium melting at the temperature about 10% higher than the real value [47].

Figure 7 shows the simulated room-temperature isotherm of α-U. The P–V dependence was traced over several independent MD calculations carried out at the given ratios V/V_0. In such a manner all stress components were kept equal: $P_{\rm xx} = P_{\rm yy} = P_{\rm zz} = P$ in each of the calculation points. It is observed that the isotherm repeats the prediction made with the U potential [31] pretty well and agrees with the set of experimental data resulting from room-temperature compression of α-U via diamond-anvil cells (DAC) [47–49]. Using MD with the potential proposed we also reproduce the experimentally measured pressure–temperature–volume (P–T–V) dependence for the orthorhombic α-U. In [50] x-ray diffraction experiments were conducted under well-controlled P–T conditions, and the corresponding lattice constants together with the atomic volume were defined. The whole list of the observed P–T–V
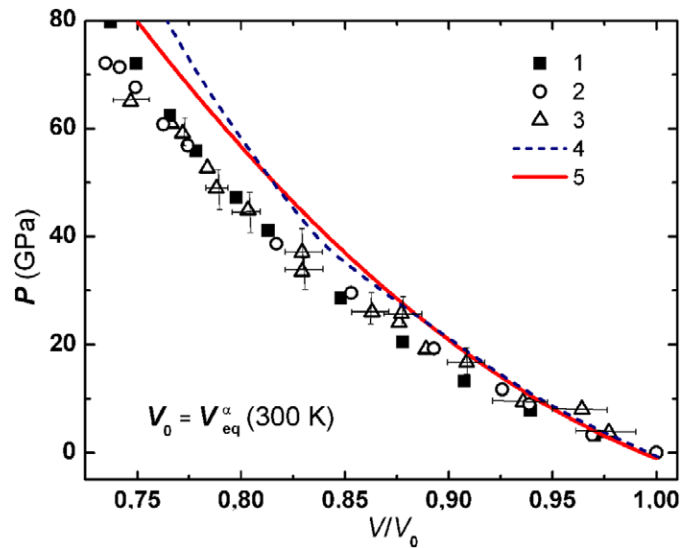
Figure 7. Room-temperature isotherm of α-U: 1, 2, 3—experimental results [47–49]; 4—result of MD calculations with the potential for pure U [31]. 5—simulation with the potential for U–Mo–Xe.
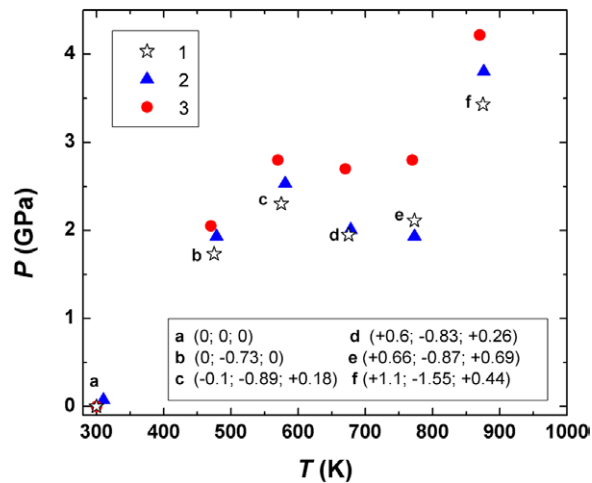

Figure 8. Pressure-temperature dependence for α-U at $V \approx V(300\,\mathrm{K})$. 1—experimental high pressure–temperature diffraction study [50]. 2—simulation with the potential for pure U [31]. 3—this work. The separate legend in the right corner of the picture contains strain values (ε_{xx}; ε_{yy}; ε_{zz}) for each point, in %.

data values is given in [50]. In the provided MD simulations the T and the $a(T)/a(300)$, $b(T)/b(300)$, $c(T)/c(300)$ and $V(T)/V(300)$ ratios in each temperature point were kept strongly equal to those measured in the experiment. The pressure values were recorded as the output of MD runs with 4000 atoms in a simulation box. The data points gathered from this simulation are plotted in figure 8 together with the experimental data. The separate legend in the right corner of the picture shows the strain values ε_{xx}, ε_{yy} and ε_{zz} in each calculation point

Table 3. Structure, elastic constants and melting temperature of pure molybdenum.

	EAM, this work	EAM Mo–Xe [30]	EAM [52]	EAM [51]	Experiment [79, 80]
a	3.1474	3.1470	3.1471	3.1465	3.1472
c_{11}	538	550	420	490	465
c_{12}	237	220	170	169	176
T_{m}	2690	2630	—	3350	2890

Note: The lattice parameter (a, provided at T near 0 K) is given in Å, and room-temperature elastic constants c_{ij} are in GPa. Melting temperature T_{m} is in kelvin.
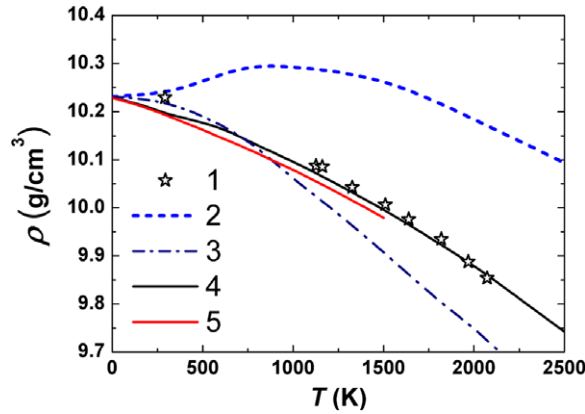
Figure 9. Thermal expansion of pure Mo at zero pressure. 1—experiment [79]. 2, 3—EAM potentials [51, 52]. 4—potential for the binary Mo–Xe system [30]. 5—this work.

estimated (in %) as

$$\varepsilon_{xx}(T) = \frac{a(T) - a(300)}{a(300)} \times 100, \tag{8}$$

$$\varepsilon_{yy}(T) = \frac{b(T) - b(300)}{b(300)} \times 100, \tag{9}$$

$$\varepsilon_{zz}(T) = \frac{c(T) - c(300)}{c(300)} \times 100, \tag{10}$$

where a, b and c are the lattice constants of α-U and T is the temperature. Figure 8 also shows the difference between EAM U–Mo–Xe and EAM U [31] performance, but both examined potentials describe this property rather well.

3.2. Calculation of pure molybdenum properties

The other extreme significant case in the study of the U–Mo–Xe system is the investigation of the properties of pure molybdenum. From table 3, which contains lattice and elastic characteristics of Mo one can see that the EAM Mo potential implemented in EAM U–Mo–Xe describes its structure well. Elastic constants deviate from the experimental values at ∼30%, while the calculations with the EAM Mo–Xe potential give a better description of c_{11} and c_{12}.

During the verification the thermal expansion of pure Mo was evaluated. Corresponding data (for zero pressure and temperatures up to 2500 K) are plotted in figure 9. The EAM U–Mo–Xe shows good agreement with the experimental curve, as well as with the previously
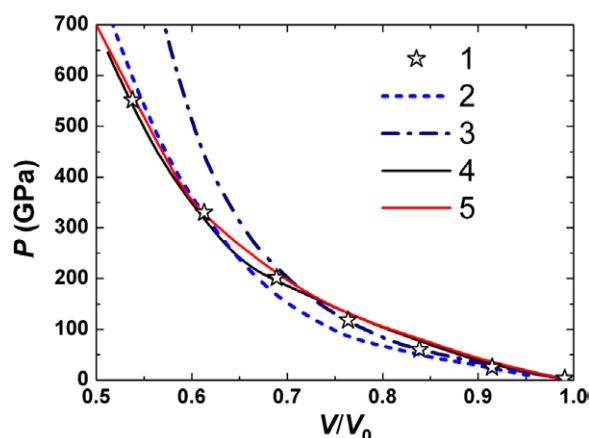
14

Figure 10. The room-temperature isotherm of molybdenum: 1—experiment [53]; 2,3,4—result of MD calculations with the EAM potentials for Mo [30, 51, 52]; 5—simulation with the potential for U–Mo–Xe. $V_0 = V(300\,\text{K})$.

developed binary EAM Mo–Xe potential. In contrast, simulations taken with the EAM potentials for Mo introduced by Derlet [51] and Finnis and Sinclair [52] are also presented and proved to give insufficient description of thermal expansion at high temperatures.

A comparison between the experimental room-temperature compression data and computed isotherms also shows that the potential provides better agreement with the experiment [53] than other widely used molybdenum potentials [51, 52]. Figure 10 proves that the dependence obtained in this work pretty much overlays with the room-temperature isotherm calculated with the Mo–Xe EAM potential [30].

3.3. Calculation of pure xenon properties

During the work on the verification of the repeatability of pure xenon properties the computations of solid and disordered xenon were performed. Considering the situation of the EAM Xe potential implemented in the resulting EAM U–Mo–Xe model it should be emphasized that because of rather small r_{cut} it is not appropriate for investigating cold low-density Xe states with large interatomic distances. To test the behaviour of cold fcc Xe under compression we compute the room-temperature isotherm. A simulation was performed with 4000 atoms of fcc Xe; the temperature was kept constant (270 K). The isotherm is plotted in figure 11 along with the other existing data including experimentally measured points [54–56], and the simulation results reported in [43], where the interatomic potential for xenon was adopted in exp-6 format. As one can see, the present results are slightly above the experimental points and the curve obtained with the Xe exp-6 potential. But the less the volume, the better is agreement. We found that our calculations appear to match the recent x-ray diffraction study [56] very well. To sum up, the room-temperature isotherm is reproduced with good accuracy, which confirms the suitability of the potential for solving the problems dealing with the fcc xenon under high pressures.

The exp-6 Xe potential was previously used to predict the high-temperature P–V dependence for disordered xenon at low densities. Note that this potential model aimed at pure Xe has a significantly larger cut-off: 14 Å. After analyses of the same P–V dependence obtained in this work, we conclude that our model compares rather well with the exp-6
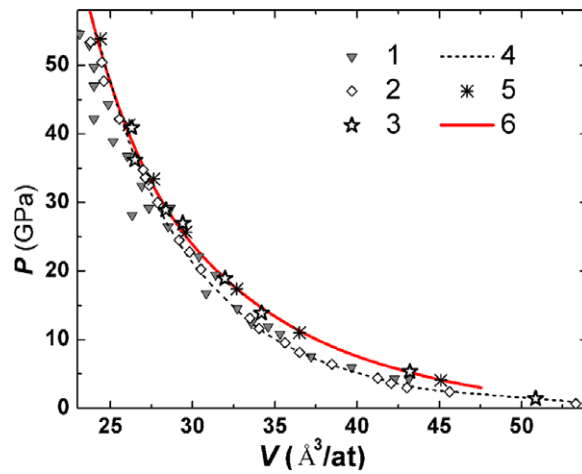
Figure 11. Room-temperature isotherm of fcc xenon. 1—Experimental data measured by DAC [54]; 2 and 3—recent experimental diamond-anvil cell measurements [55] and [56]; 4—simulation with exp-6 potential [43]; 5—simulation with EAM Mo–Xe [30]; 6—results of this work.
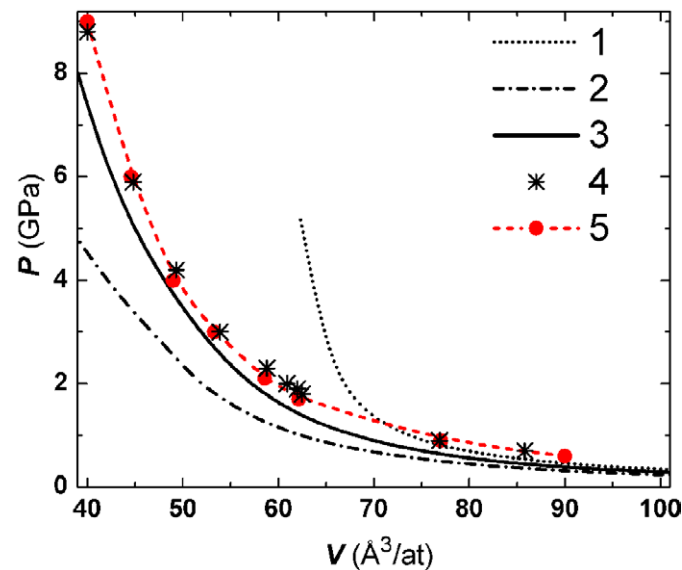

Figure 12. Pressure-volume dependence for liquid xenon at 900 K. 1—EOS Kaplun [87]; 2—EOS Ronchi [88]; 3—MD simulations with exp-6 potential [89]; 4—MD simulations with Mo–Xe potential [30]; 5—results of this work.

predictions (see figure 12 where some data derived from the theoretical equations of state for Xe are also indicated). Continuing the evaluation of our model among the experimental and exp-6 potential data, the melting line at the pressures up to 25 GPa was traced (figure 13).

The information gathered in this subsection shows that the developed EAM Xe potential is applicable for the simulation of xenon. This conclusion is based on a satisfactory comparative study between the present potential, exp-6 form, theoretical and experimental results existing for xenon.
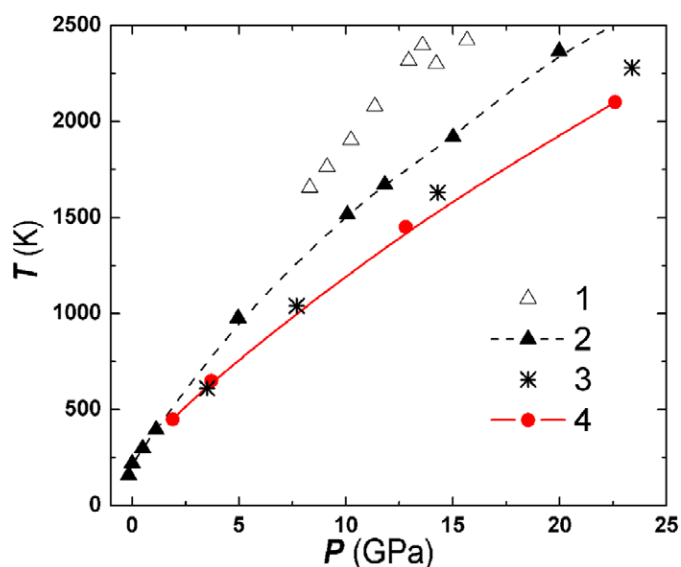
16

Figure 13. Melting temperatures of fcc xenon at pressure up to 25 GPa. 1—Experimental data [90, 91]; 2—simulation with exp-6 Xe interatomic potential [43]; 3—dependence calculated using the EAM Mo–Xe potential; 4—result of this work.

4. Calculation of the characteristics of the binary U–Mo system: U–10 wt%Mo alloy, U_2Mo intermetallic and U–Mo solid solutions

The main purpose of the potential development is to obtain an opportunity to study γ-U–Mo fuel and their possible modifications using MD. Here we present the calculation results for some general characteristics of the most prominent U–10 wt% Mo alloy and U_2Mo intermetallic. According to the reported data, the addition of 10 wt% (or 21.6 at%) of molybdenum to uranium leads to the formation of a substitutional solution with bcc structure, where the lattice parameter equals a (see the first example in figure 1).

To create the random distribution of substitutional Mo atoms in the equilibrium U–10 wt%Mo alloy the preliminary simulation procedure was adopted. The full size of the initial model was set to be 2000 atoms (90 wt% of U, 10 wt% of Mo), with Mo substitutional atoms ordered in some given way. Then to drive out the Mo order the model was heated to 1500 K and relaxed at high temperature for several tens of ns. After heating, the system was cooled, and the main relaxation stage was provided at 800 K. The temperature was kept constant via a Langevin thermostat. The simulation continued until the average potential energy value became constant and did not change in time. The decrease in the potential energy takes about 0.4 μs ($\sim 4 \times 10^8$ MD steps, one step equals 10^{-3} ps). According to figure 14 one might estimate the resulted structure by comparison of its radial-distribution functions with the one computed for U in pure γ-U at the same lattice parameter. All the indicated peaks for U–U, U–Mo, Mo–Mo in U–10 wt%Mo and U–U in pure bcc U appear at the same distances, and the distribution functions are found to be quite similar. The following calculations dealing with U–10 wt%Mo properties were taken using this preliminary relaxed structure containing 2000 atoms.

In the case of two-phase melting computations the cubic model with 2000 atoms was replicated six times in one direction to come to a parallelepiped containing 12 000 atoms.
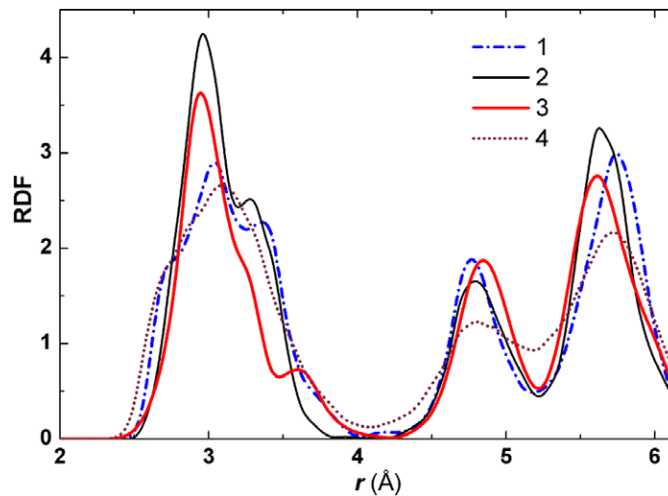
Figure 14. Radial-distribution function calculated for U–10Mo model at 300 K: 1—for U–U, 2—for U–Mo, 3—for Mo–Mo; 4—RDF calculated for bcc U at the same lattice parameter and $T = 900$ K, introduced for comparison.

Table 4. Structure and elastic properties of U–10 wt%Mo alloy and U$_2$Mo at 300 K and 0 GPa.

	EAM, this work	Experiment
	U–10 wt%Mo	
a (300 K)	3.407	3.4129 [81]; 3.4213 [20]
a (800 K)	3.417	3.44
T_{m}	1500	1455 [20]
E	76	65 [15], 60–71 [13], 69.8 [82], 82.9–91.5 [83], 87.1 [84]
α(300–800 K)	6.7	11.5–16.7 [60]; 1–15 [57]
	U$_2$Mo	
a_1	3.422	3.426 [62]
a_2	3.325	3.426
c	9.888	9.834

Note: All lattice constants are presented in Å. Reference values for U–10 wt%Mo lattice parameters are given in [20, 81]. In the case of U$_2$Mo two lattice parameters that should be equal to a are denoted as a_1 and a_2 because of the difference in their values. Young's modulus E of U–10 wt%Mo is in GPa, T_{m} is in K and the thermal expansion coefficient $\alpha(T)$ is in 10^{-6} K^{-1}.

The melting temperature of U–10 wt%Mo at zero pressure is predicted to be sufficiently near the value determined from the phase diagram of the U–Mo system [11, 13]. The study undertaken here proves that the model structure of the U–10 wt%Mo alloy built with the proposed U–Mo–Xe potential remains stable in an appropriate temperature range: from 300 K up to the melting point (∼1500 K).

Elastic properties of the fuel model were examined by the computation of the modulus of elasticity E at 300 K. It was found to be close to the results of engineering stress–strain experiments. The difference between the experimental Young's modulus summarized in table 4 arises from the different geometry of the sample used together with the different order of the heat treatment. The most recent experiments mentioned above provide mechanical testing of the fuel foils. We also use our model to estimate the density of the simulated alloy. At 300 K
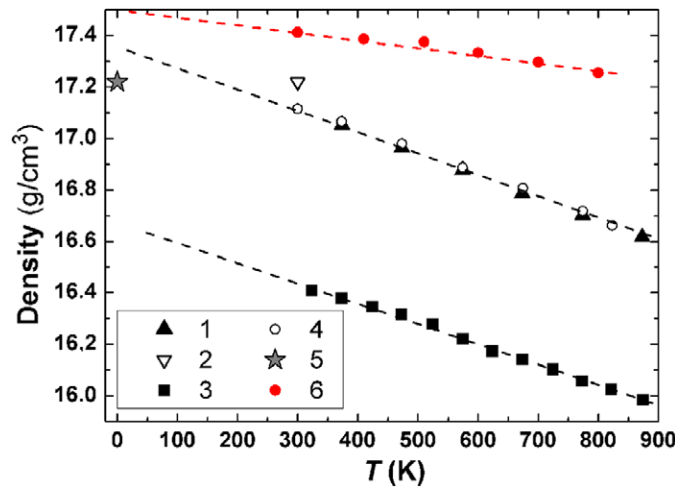
Figure 15. Density of the U–10Mo alloy. 1,2,4—experimental study [58–60] respectively; 3—recent experimental measurements [57]; 5—theoretical prediction obtained from the atomic volume calculated in [23] at 0 K; 6—results of the MD simulation with the potential for U–Mo–Xe.

it appears to be about $17.4 \, \mathrm{g \, cm^{-3}}$ (see figure 15), while the experimental measurements for U–10 wt%Mo produce data in the interval from 16 [57] to $17.2 \, \mathrm{g \, cm^{-3}}$ [58, 59] depending on the porosity presence (in [57] it is considered to be significant).

We have also traced how the lattice constant of bcc U–10 wt%Mo changes with the temperature to obtain the thermal expansion coefficient. The lattice parameters for 300 and 800 K are given in table 4. They allow us to estimate the average linear thermal expansion coefficient at 300–800 K to be about $6.7 \times 10^{-6} \, \mathrm{K^{-1}}$, about two times lower than the experimentally provided values. According to Klein [60], thermal expansion of U–10 wt%Mo should change from 11.5×10^{-6} to $16.7 \times 10^{-6} \, \mathrm{K^{-1}}$ in the same temperature interval. Those measurements are proved by the recent experimental study on U–10 wt%Mo [57], which stated that $\alpha(300 \, \mathrm{K}) = 10 \times 10^{-6} \, \mathrm{K^{-1}}$ and for 800 K it is $15 \times 10^{-6} \, \mathrm{K^{-1}}$. This comparison leads us to conclude that in spite of the fact that the interatomic potential gives an accurate description of lattice parameter a at 300 K, it underestimates the thermal expansion coefficient.

Speaking of the possible modifications of the U–Mo fuel, we kept in mind that one of the most possible fuel structure changes can be provoked by the decomposition of bcc γ-U–Mo into the mixture of orthorhombic α-U and ordered intermetallic U_2Mo. The tendency of nucleation of the ordered U_2Mo compound and low-temperature orthorhombic α-U in the metastable γ-U–Mo under irradiation is experimentally observed at $T \leqslant 900 \, \mathrm{K}$. Using MD with the potential for U–Mo–Xe we examined whether it is suitable to investigate the U_2Mo compound and α-U–Mo, in spite of the fact that none of these structures have been included in the reference database during the potential derivation (see table 1). Originally, real U_2Mo is a $MoSi_2$-type intermetallic compound, where two lattice constants equal a and the third one equals c ($c/a = 2.876$) [61, 62]. The model structure of U_2Mo built with the EAM U–Mo–Xe potential turns out to be slightly deformed. We observe some lattice distortion of the ideal tetragonal structure leading to the difference in the lattice constants that originally should be equal to a (see table 4). Note that despite this all lattice constants conform well to the experimental data. The potential was also tested for the ability to reproduce stable solid α-U–Mo solutions existing in the U–Mo phase diagram at low temperatures up to 1.5–2 at% of Mo (see [11]). A number of computations were performed for the α-U structure with 0.4,

0.7, 1.2 and 4.2 at% of U atoms substituted by Mo. In all cases the structure remains stable at 300 K for the entire time of the observations (16 ns for each MD run).

The list of the results proves that the potential provides various levels of accuracy while simulating various characteristics of U–10 wt%Mo, U_2Mo and α-U–Mo solid solutions. Nevertheless, we can conclude that the overall quality of the material representation is rather satisfactory and allows for possibility of the investigation of these significant phases in the U–Mo system.

5. Single defect properties of pure uranium and molybdenum

The potential was designed primarily for the investigation of the defects generated in U–Mo alloys by radiation or fission products. The predictive ability of the MD method can be useful here due to a scarcity of experimental and theoretical data on the structure and mobility of radiation defects in γ-U–Mo alloys. This implies that there are no evident data for the direct verification of the potential by analyses of defect formation and migration in the U–Mo alloy. Hence, the starting point in this field was the verification of single point-defect properties in pure U and Mo.

We calculate a single point defect formation energy for solid γ-uranium and molybdenum. This energy is determined as follows, for vacancy:

$$E_{vac}^f = E_{n-1} - \frac{n-1}{n}E_n,\tag{11}$$

and for SIA:

$$E_{SIA}^f = E_{n+1} - \frac{n+1}{n}E_n.\tag{12}$$

Here n is the number of atoms in the model of the crystal lattice without any defect. E_n is the energy of this lattice, E_{n-1} corresponds to the model that contains a single vacancy, E_{n+1} is the energy of the structure with one additional SIA. We have performed structural relaxations for the models of γ-U and Mo with a single vacancy/SIA to determine the energy values E_{n-1} and E_{n+1}, respectively.

Formation energies of defects in γ-U are estimated at finite temperatures from the energies averaged along a long molecular dynamic trajectory in the NVT ensemble. With the potential for U–Mo–Xe we have obtained that the U-vacancy formation energy varies from approximately 2.2 eV at 500 K to 3 eV at 1500 K. A similar increase in the U-vacancy formation energy (from 1.8 to 2.3 eV) is reported in [63] from the classical MD with the modified EAM potential. The values from the MD simulations are overestimated in comparison with the data [64, 65] obtained both in DFT static calculations (approximately from 1.1 to 1.4 eV—see table 6 for details) and in positron annihilation experiments (approximately 1.2 eV).

Uranium self-interstitial formation energy is around 1.05 eV and is nearly temperature independent (according to MD simulations with the U–Mo–Xe potential). This value agrees well with the estimates from the DFT static calculations: from 0.5 to 1.5 eV depending on the configuration [65]. One might note that the formation energies of the intrinsic interstitials and vacancies in γ-U are quite close to each other; hence both are able to contribute to a self-duffusion coefficient. Moreover, our MD simulations of the diffusion of point defects show that the U-SIA are substantially more mobile than the vacancies. The sum of SIA formation (1.05 eV) and migration (around 0.15 eV) energies is quite close to the activation energy of self-diffusion 1.15 eV reported in experiments [66].

The self-interstitial atom formation energies for pure molybdenum in the form of relative formation energies of six possible defect configurations are plotted in figure 16, here

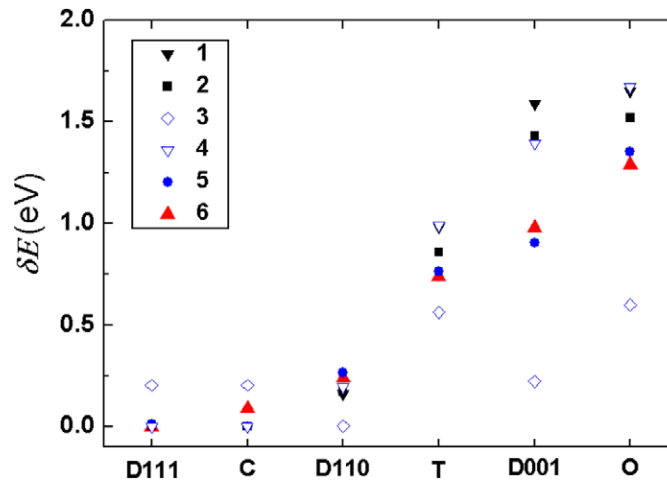$$\delta E = E^f - E_{min}^f,\tag{13}$$

20

Figure 16. SIA formation energies for Mo (relative to the minimum value for each of the potentials). 1,2—DFT predictions [67, 68]; 3,4,5—values calculated with EAM potentials [30, 51, 52]; 6—result obtained in this work.

Table 5. The energy of a single-vacancy formation in molybdenum (eV).

EAM, this work	EAM [30]	*Ab initio* [68]	Experiment [85]
2.61	2.79	2.96	2.6–3.2

Table 6. The energy of a single-vacancy formation in γ-U (eV).

EAM, this work	MEAM [63]	*Ab initio* [64]	*Ab initio* [65]	EAM [31]	DFT-MD, this work	Expt. [86]
2.2–3.0	1.8–2.3	1.08	1.384	1.52	1.3	1.20 ± 0.25

and $E_{\min}^{\mathrm{f}}$ is the minimal formation energy of SIA configuration (dumbbell $\langle 1\,1\,0 \rangle$ in the case of EAM U–Mo–Xe). The figure shows that the potential can describe the hierarchy of defect energies in agreement with the one calculated within the DFT in [67, 68]. From table 5 we can also see that the estimated vacancy formation energy for pure Mo agrees well with the existing DFT and experimental data.

6. Conclusions

The study presented here is the first attempt to provide MD simulation of U–Mo fuel alloys. To perform the investigations a new EAM interatomic potential for the U–Mo–Xe system is proposed. It is fitted to the *ab initio* data and tested by the calculation of the general properties of the U, Mo, Xe, U–Mo alloys and U_2Mo intermetallic. The results obtained for the elastic constants, thermal expansion, room-temperature isotherm and melting temperature of all the phases studied are consistent with the experimental data. The single defect (vacancy, SIA) formation energies in U and Mo agree with the results of *ab initio* calculations. The potential is proved to be able to reproduce the stable structure, modulus of elasticity, room-temperature density and melting temperature of U–10 wt%Mo, while thermal expansion of the alloy model is found to be about two times lower than the experimental values. The verification results

lead us to conclude that the potential proposed provides the opportunity to analyse various complicated processes taking place in the ternary U–Mo–Xe system.

One of the most important applications of the developed interatomic potential is the modelling of defect evolution in U–Mo alloys on the atomistic scale. This problem is a matter of great interest in nuclear engineering but, in spite of this, many questions existing in the field still remain open. They deal with single-point defect formation and evolution and with large-scale structure changes. For example, the latter can be related to the processes of the voids (or fission gas bubbles) superlattice formation experimentally observed for U–Mo fuel by Rest *et al* and Gan *et al* [69–71]. These phenomena have not been made clear and can be studied using MD. The potential proposed can be applied to the investigation of structural and phase transitions caused by the passage of a high-energy ion through the fuel material. The detailed atomistic simulations of the processes described above are to be carried out in future. The potential is supposed to be used to expand our knowledge about the processes existing in the U–Mo fuel compositions under irradiation together with corresponding changes in the fuel structure and strength properties. The resulting data can be deployed as an input for the theoretical models of the long time evolution of damaged material [72–75].

Acknowledgments

References

[1] Hofman G L, Walters L C and Bauer T H 1997 *Prog. Nucl. Energy* **31** 83–110
[2] Meyer M 2002 *J. Nucl. Mater.* **304** 221–36
[3] Kim Y S, Hofman G and Yacout A 2009 *J. Nucl. Mater.* **392** 164–70
[4] Carmack W J, Porter D L, Chang Y I, Hayes S L, Meyer M K, Burkes D E, Lee C B, Mizuno T, Delage F and Somers J 2009 *J. Nucl. Mater.* **392** 139–50
[5] Wirth B D 2007 *Science* **318** 923–4
[6] Bai X M, Voter A F, Hoagland R G, Nastasi M and Uberuaga B P 2010 *Science* **327** 1631–4
[7] Sivak A, Romanov V and Chernov V 2010 *Crystallogr. Rep.* **55** 97–108
[8] Stewart D, Osetsky Y, Stoller R, Golubov S, Seletskaia T and Kamenski P 2010 *Phil. Mag.* **90** 97–108
[9] Malerba L *et al* 2010 *J. Nucl. Mater.* **406** 7–18
[10] Kalin B, Yakushin V, Dzhumaev P, Polskii V, Golovchanskii I, Fedotov V, Sevryukov O and Suchkov A 2011 *Inorg. Mater.: Appl. Res.* **2** 218–23
[11] Kim Y 2012 *Comprehensive Nuclear Materials, vol 3: Advanced Fuels/Fuel Cladding/Nuclear Fuel Performance Modeling and Simulation* (Amsterdam: Elsevier)
[12] Sinha V, Hegde P, Prasad G, Dey G and Kamath H 2010 *J. Alloys Compounds* **506** 253–62
[13] Burkes D, Prabhakaran R, Hartmann T, Jue J F and Rice F 2010 *Nucl. Eng. Des.* **240** 1332–39
[14] Burkes D, Wachs D, Keiser D, Okuniewski M, Jue J F, Rice F and Prabhakaran R 2009 INL/CON-09-15633 preprint: Update on Fresh Fuel Characterization of U–Mo Alloys Technical Report
[15] Ozaltun H, Herman Shen M H and Medvedev P 2011 *J. Nucl. Mater.* **419** 76–84
[16] Vatulin A, Morozov A, Suprun V, Petrov Y I and Trifonov Y I 2004 *Met. Sci. Heat Treatment* **46** 484
[17] Park J M, Kim K H, Kim C K, Meyer M, GL H and Strain R 2001 *Met. Mater. Int.* **7** 151–7

[18] Keiser D, Hayes S, Meyer M and Clark C 2003 *JOM J. Min. Met. Mater. Soc.* **55** 55–58
[19] Baranov V, Nechaev V, Produvalov B and Shornikov D 2010 *At. Energy* **108** 349–56
[20] Sinha V, Prasad G, Hegde P, Dey G and Kamath H 2010 *J. Alloys Compounds* **491** 753–60
[21] Kim Y-S H G, Yacout A and Kim T K 2009 *Proc. Int. Conf. Fast Reactors and Related Fuel Cycles (FR09),
       Challenges and Opportunities, 1 A E A-CN-176 (Kyoto, Japan)* pp 1–9
[22] Huang G Y and Wirth B 2012 *J. Phys.: Condens. Matter* **24** 415404
[23] Landa A, Soderlind P and Turchi P 2011 *J. Nucl. Mater.* **414** 132–7
[24] Govers K, Lemehov S, Hou M and Verwerft M 2007 *J. Nucl. Mater.* **366** 161–77
[25] Govers K, Lemehov S, Hou M and Verwerft M 2008 *J. Nucl. Mater.* **376** 66–77
[26] Yakub E, Ronchi C and Staicu D 2007 *J. Chem. Phys.* **127** 094508
[27] Potashnikov S, Boyarchenkov A, Nekrasov K and Kupryazhkin A 2011 *J. Nucl. Mater.* **419** 217–25
[28] Daw M and Baskes M 1984 *Phys. Rev.* B **29** 6443–53
[29] Belashchenko D K 2012 *High Temp.* **50** 331–9
[30] Starikov S, Insepov Z, Rest J, Kuksin A Y, Norman G, Stegailov V and Yanilkin A 2011 *Phys. Rev.* B **84** 104109
[31] Smirnova D, Starikov S and Stegailov V 2012 *J. Phys.: Condens. Matter* **24** 015702
[32] Ercolessi F and Adams J B 1994 *Europhys. Lett.* **26** 583–8
[33] Plimpton S J 1995 *J. Comput. Phys.* **117** 1
[34] Kresse G 1996 *Phys. Rev.* B **54** 11169–86
[35] Brommer P and Gähler F 2006 *Phil. Mag.* **86** 753–8
[36] Fellinger M R, Park H and Wilkins J W 2010 *Phys. Rev.* B **81** 144119
[37] Li J, Bursten B E, Liang B and Andrews L 2002 *Science* **295** 2242
[38] Johnson R A 1989 *Phys. Rev.* B **39** 12554–9
[39] Williams P, Mishin Y and Hamilton J 2006 *Modelling Simul. Mater. Sci. Eng.* **14** 817–33
[40] Li Y, Shan T R, Liang T, Sinnott S B and Phillpot S R 2012 *J. Phys.: Condens. Matter* **24** 235403
[41] Pascuet M, Bonny G and Fernandez J 2012 *J. Nucl. Mater.* **424** 158–63
[42] Dai Y, Lu C, Ren Q, Lu L, Li J and Li B 2012 *J. Nucl. Mater.* **427** 239–44
[43] Belonoshko A B, LeBacq O, Ahuja R and Johansson B 2002 *J. Chem. Phys.* **117** 7233
[44] Morris J, Wang C, Ho K and Chan C 1994 *Phys. Rev.* B **49** 3109–15
[45] Starikov S V and Stegailov V V 2009 *Phys. Rev.* B **80** 220104(R)
[46] Belonoshko A 1994 *Geochim. Cosmochim. Acta* **58** 4039–47
[47] Yoo C S, Cynn H and Söderlind P 1998 *Phys. Rev.* B **57** 10359–62
[48] Akella J, Smith G S, Grover R, Wu Y and Martin S 1990 *High Pressure Res.* **2** 295–302
[49] Le Bihan T, Heathman S and Idiri M 2003 *Phys. Rev.* B **67** 134102
[50] Zhao Y, Zhang J, Brown D, Korzekwa D, Hixson R and Wang L 2007 *Phys. Rev.* B **75** 174104
[51] Derlet P M, Nguyen-Manh D and Dudarev S L 2007 *Phys. Rev.* B **76** 054107
[52] Finnis M W and Sinclair J E 1984 *Phil. Mag.* A **50** 45
[53] Vohra Y and Ruoff A 1990 *Phys. Rev.* B **42** 8651–4
[54] Zisman A, Alexandrov I and Stishov S 1985 *Phys. Rev.* B **32** 484–7
[55] Cynn H, Yoo C S, Baer B, Iota-Herbei V, McMahan A K, Nicol M and Carlson S 2001 *Phys. Rev. Lett.* **86** 4552–5
[56] Errandonea D, Schwager B, Boehler R and Ross M 2002 *Phys. Rev.* B **65** 1–6
[57] Burkes D E, Papesch C A, Maddison A P, Hartmann T and Rice F J 2010 *J. Nucl. Mater.* **403** 160–6
[58] Bridge J, Schwartz C and Vaughan D 1956 *Trans. AIME* **206** 1282
[59] McGeary R 1955 Development and properties of uranium-based alloys resistant to corrosion in high-temperature
       water *SAEC Report* WAPD-127-part 1 Technical Report
[60] Klein J 1962 *Uranium and its Alloys Nuclear Reactor Fuel Elements: Metallurgical Fabrication* (New York:
       Interscience)
[61] Halteman E 1957 *Acta Crystallogr.* **10** 166–169
[62] Kutty T, Dash S, Banerjee J, Kaity S, Kumar A and Basak C 2012 *J. Nucl. Mater.* **420** 193–7
[63] Beeler B, Deo C, Baskes M and Okunewski M 2012 *J. Phys.: Condens. Matter* **24** 075401
[64] Xiang S, Huang H and Hsiung L 2008 *J. Nucl. Mater.* **375** 113–9
[65] Beeler B, Good B, Rashkeev S, Deo C, Baskes M and Okuniewski M 2010 *J. Phys.. Condens. Matter* **22** 505703
[66] Peterson N L and Rothman S J 1964 *Phys. Rev.* **136** A842–8
[67] Han S, Zepeda-Ruiz L A, Ackland G J, Car R and Srolovitz D J 2002 *Phys. Rev.* B **66** 220101(R)
[68] Nguyen-Manh D, Horsfield A P and Dudarev S L 2006 *Phys. Rev.* B **73** 020101
[69] Rest J, Hofman G and Kim Y S 2009 *J. Nucl. Mater.* **385** 563–71
[70] Gan J, Keiser J, Wachs D, Robinson A, Miller B and Allen T 2010 *J. Nucl. Mater.* **396** 234
[71] Gan J, Keiser D Jr, Miller B, Robinson A, Jue J, Medvedev P and DM W 2012 *J. Nucl. Mater.* **424** 43–50
[72] Rest J and Hofman G L 2000 *J. Nucl. Mater.* **277** 231

[73] Yanilkin A V, Insepov Z, Norman G E, Rest J and Stegailov V V 2012 *Defect Diffusion Forum* **323–325** 95–100
[74] Insepov Z, Rest J, Yacout A M, Kuksin A Y, Norman G E, Stegailov V V, Starikov S V and Yanilkin A V 2012
        J. Nucl. Mater. **425** 41–7
[75] Veshchunov M, Dubourg R, Ozrin V, Shestak V and Tarasova V 2007 *J. Nucl. Mater.* **362** 327–36
[76] Barrett C, Mueller M and Hitterman R 1963 *Phys. Rev.* **129** 625–9
[77] Soderlind P 1998 *Adv. Phys.* **47** 959
[78] Dabos S, Dufour C, Benedict U and Page M 1987 *J. Magn. Magn. Mater* **63-64** 661
[79] Edwards J, Speiser R and Johnston H 1951 *J. Appl. Phys.* **22** 424
[80] Errandonea D, Schwager B, Ditz R, Gessmann C, Boehler R and Ross M 2001 *Phys. Rev.* B **63** 132104
[81] Dwight A 1960 *J. Nucl. Mater.* **2** 81
[82] Burkes D, Prabhakaran R, Jue J F and Rice F 2009 *Metall. Mater. Trans.* A **40** 1069–79
[83] Nomine A, Bedere D and Miannay D 1974 Physical metallurgy of uranium alloys *Proc. 3rd Army Materials
        Technical Conf. (Vail, CO)* ed J Burke *et al* pp 657–99
[84] Waldron M, Burnett R and Pugh S 1958 AERE-M/B-2554 Technical Report
[85] Ullmaier H (ed) 1991 *Landolt-Borstein Numerical Data and Functional Relationships in Science and Technology,
        Group III, vol 25, Atomic Defects in Metals* (Berlin: Springer)
[86] Matter H, Winter J and Triftshauser W 1980 *J. Nucl. Mater.* **88** 273–8
[87] Kaplun A and Meshalkin A 2003 *Thermophys. Prop. Mater.* **41** 373
[88] Ronchi C 1981 *J. Nucl. Mater.* **96** 314
[89] Oh J Y, Koo Y H, Cheon J S, Lee B H and Sohn D S 2008 *J. Nucl. Mater.* **372** 89–93
[90] Ross M, Boehler D, Boercker D and P S 1999 *Int. Conf. on High Pressure Science and Technology (AIRAPT-17)
        (Honolulu, HI)* 195
[91] Boehler R, Ross M, Soderlind P and Boercker D 2001 *Phys. Rev. Lett.* **86** 5731